Hydroelastic interaction between water waves and an array of circular floating porous elastic plates

Siming Zheng[1],[†], **Michael H. Meylan**[2], **Guixun Zhu**[1], **Deborah Greaves**[1] and **Gregorio Iglesias**[1],[3]

[1]School of Engineering, Computing and Mathematics, University of Plymouth, Drake Circus, Plymouth PL4 8AA, UK

[2]School of Mathematical and Physical Sciences, The University of Newcastle, Callaghan 2308, Australia

[3]MaREI, Environmental Research Institute and School of Engineering, University College Cork, Cork P43 C573, Ireland

A theoretical model based on linear potential flow theory and an eigenfunction matching method is developed to analyse the hydroelastic interaction between water waves and multiple circular floating porous elastic plates. The water domain is divided into the interior and exterior regions, representing the domain beneath each plate and the rest, which extends towards infinity horizontally, respectively. Spatial potentials in these two regions can be expressed as a series expansion of eigenfunctions. Three different types of edge conditions are considered. The unknown coefficients in the potential expressions can be determined by satisfying the continuity conditions for pressure and velocity at the interface of the two regions, together with the requirements for the motion/force at the edge of the plates. Apart from the straightforward method to evaluate the exact power dissipated by the array of porous elastic plates, an indirect method based on Green's theorem is determined. The indirect method expresses the wave-power dissipation in terms of Kochin functions. It is found that wave-power dissipation of an array of circular porous elastic plates can be enhanced by the constructive hydrodynamic interaction between the plates, and there is a profound potential of porous elastic plates for wave-power extraction. The results can be applied to a range of floating structures but have special application in modelling energy loss in flexible ice floes and wave-power extraction by flexible plate wave-energy converters.

Key words: wave–structure interactions, surface gravity waves, wave scattering

1. Introduction

In recent years, due to industrial and residential applications, the demand for the development and utilisation of artificial marine structures nearshore and offshore has increased significantly (Lamas-Pardo, Iglesias & Carral 2015). Among the wide variety of nearshore and offshore artificial structures, some can be identified as floating porous

† Email address for correspondence: siming.zheng@plymouth.ac.uk

elastic plates with small draught relative to their horizontal dimensions, e.g. floating flexible breakwaters (Michailides & Angelides 2012), artificial floating vegetation fields (Kamble & Patil 2012) and extensive aquaculture farms (Wang & Tay 2011). The floating elastic plate model is the basis for understanding this process (Squire 2020). In particular, the scattering characteristics are best analysed by considering multiple ice floes to account for interactions (Bennetts *et al.* 2010; Montiel, Squire & Bennetts 2015*a*, 2016; Montiel & Squire 2017). However, these elastic plate scattering models cannot account for the loss of energy, and there are several models which propose that a porous or equivalent layer can account for the observed energy loss (Zhao & Shen 2018; Sutherland *et al.* 2019). These models motivate the study of flexural deformations of floating porous elastic plates subject to water waves and to evaluate carefully the wave-energy dissipation caused by their porosity.

The water-wave scattering of floating elastic plates has been comprehensively investigated by numerous researchers, and there are several reviews that relate to this topic (e.g. Squire 2008, 2011, 2020). To evaluate the interaction of waves with a horizontal floating semi-infinite elastic plate, Sahoo, Yip & Chwang (2001) used the analytic representation based on the eigenfunction expansion method of Fox & Squire (1994), in the context of two-dimensional (2-D) linear potential flow theory. The influence of various edge conditions, i.e. a free edge, a simply supported edge and a built-in edge, on the hydrodynamic behaviour was investigated. The free-edge condition was shown to result in the maximum plate deflection. Squire & Dixon (2000) studied wave propagation across a narrow straight-line crack in an infinite thin plate floating on water of infinite depth with a Green's function model. The reflection and transmission coefficients were observed to depend significantly on the wave frequency. Evans & Porter (2003) provided an explicit solution for the wave scattering of an infinite thin plate with a crack for finite water depth. They obtained a more straightforward approach by splitting the higher-order conditions to be satisfied at the edge of each plate into the sum of even and odd solutions. These models (Squire & Dixon 2000; Evans & Porter 2003) for the single-crack problem were later extended to an elastic plate with multiple cracks (Squire & Dixon 2001; Porter & Evans 2006), but where all the plates have identical properties. Then, Kohout *et al.* (2007) studied a 2-D fluid covered by a finite number of elastic plates, which were of arbitrary characteristics. Williams & Porter (2009) introduced an eigenfunction expansion method based on deriving an integral equation, which was then solved using the Galerkin technique, to determine the problem of wave scattering by two semi-infinite plates. These two semi-infinite plates can have different properties, including variable submergence following Archimedes' principle. A similar problem was later investigated by Zhao & Shen (2013) in which the plates were considered to have viscoelastic material properties. More recently, Kalyanaraman *et al.* (2019) considered wave interactions with a land-attached elastic plate of constant thickness and non-zero draught. The solution was found to be strongly influenced by the draught. Koley, Mondal & Sahoo (2018) investigated wave scattering of a flexible plate composed of porous materials floating in water of finite and infinite depths employing the Green's function procedure. The porosity was modelled using Darcy's law, and the porous-effect parameter was taken as a complex number to account for both the resistance and inertia effects. The dissipation of the wave power due to structural porosity reduced the wave transmission on the lee side of the plate, which led to the creation of a tranquil zone.

In order to understand the hydroelastic problem of elastic plates floating in ocean waves when the plate length along the crest line of the incident waves is not much larger than the wavelength, three-dimensional effects must be considered. Meylan & Squire (1996) studied the behaviour of a solitary, circular, flexible ice floe brought into motion by the

action of long-crested sea waves. Two independent methods were developed in their model, i.e. an expansion in the eigenfunctions of a thin circular plate, and the more general method of eigenfunctions used to construct a Green's function for the plate, enabling a check to be carried out on the model. Zilman & Miloh (2000) developed a three-dimensional closed-form solution based on the angular eigenfunction expansion method for water-wave interaction with a circular thin elastic plate floating in shallow water. Their method was based on the roots of the dispersion equation. Since the shallow-water approximation was considered, only three roots in the plate-covered region and one root in open water were required in their model. The potential was matched at the edge of the plate, and the plate boundary conditions were applied to solve the wave scattering problem. Peter, Meylan & Chung (2004) extended the earlier study (Zilman & Miloh 2000) to a theoretical solution for a circular elastic plate floating in finite-depth water, i.e. without the restriction of the shallow-water approximation. Therefore, more roots of the dispersion equation for both the plate-covered region and the open-water region were required. The potential throughout the water depth, rather than at a point, was matched and the plate boundary conditions were applied. Since the plate geometry was circular (Zilman & Miloh 2000; Peter *et al.* 2004), the angular eigenfunctions can be decoupled. Hence each angular eigenfunction can be solved separately, and the matching problem becomes 2-D, similar to the method of Sahoo *et al.* (2001) and others. Montiel *et al.* (2013*a*,*b*) reported a series of wave basin experiments and analytical simulations that investigated the flexural response of one or two circular floating thin elastic plates to monochromatic waves. The plate–plate hydrodynamic interactions were observed in the two-plate tests. Recently, Meylan, Bennetts & Peter (2017) carried out an analytical study on wave scattering by a circular floating porous elastic plate. A quantity proportional to the energy dissipated by the plate due to porosity was calculated by integrating the far-field amplitude functions, but the exact dissipated power was not given. The hydroelastic characteristics of elastic plates in other situations, such as a horizontal elastic plate submerged in the water (Mahmood-Ul-Hassan, Meylan & Peter 2009; Mohapatra, Sahoo & Guedes Soares 2018*a*), a submerged horizontal flexible porous plate (Behera & Sahoo 2015; Renzi 2016; Mohapatra, Sahoo & Guedes Soares 2018*b*), submerged multilayer horizontal porous plate breakwaters (Fang, Xiao & Peng 2017), multiple floating elastic plates with a body floating or submerged in the water (Li, Wu & Ji 2018*a*,*b*) have also been investigated.

The methods used to calculate the scattering from a single body can be extended to multiple bodies, but there is a rapid growth in the computational cost. For this reason, methods based on a scattering matrix (or diffraction transfer matrix) have been developed to solve for multiple floating bodies, using the theory of Kagemoto & Yue (1986). This has been particularly true for the case of floating elastic plates used to model ice floes. The first application of this theory was by Peter & Meylan (2004) and this remains the only application of the theory to ice floes where they were not assumed circular. The circular floe case has been extended in a number of steps, first by considering arrays (Peter & Meylan 2009; Bennetts *et al.* 2010) and then to random layers using a quasi-2-D representation (Montiel *et al.* 2015*a*, 2016; Montiel & Squire 2017).

Although water-wave interaction with floating elastic plates has been widely studied, most of these plates were non-porous. Until now only a few research works on porous elastic plates have been reported, among which the investigation carried out by Koley *et al.* (2018), Meylan *et al.* (2017) and Zheng *et al.* (2020) was focused on a single porous elastic plate. For an array of such porous elastic plates, especially with the individual plates deployed close to one another, the hydrodynamic interaction between them can significantly influence their responses. To the best of the authors' knowledge, the hydrodynamic interaction between multiple floating porous elastic plates has not been

investigated yet. In this paper, a theoretical model is developed based on linear potential flow theory and an eigenfunction matching method to investigate wave scattering by multiple circular floating porous elastic plates with three different types of edge conditions, i.e. free edge, simply supported edge and clamped edge. Two methods for evaluating the exact power dissipated by the array of porous plates are proposed.

The rest of this paper is organised as follows. Section 2 outlines the mathematical model for wave scattering problem. Section 3 presents the theoretical solutions of spatial velocity potentials in the water domain. The methods for evaluating the scattered far-field amplitude function and power dissipation are supplied in § 4. Validation of the present theoretical model is presented in § 5. The validated model is then applied to carry out a multiparameter study, the results of which can be found in § 6. Finally, conclusions are outlined in § 7.

2. Mathematical model

The scattering problem of an array of circular floating porous elastic plates is considered (figure 1). The water domain is divided into two parts, (*a*) interior region, i.e. the region beneath each plate and (*b*) the exterior region, i.e. the remainder extending towards infinite distance horizontally. A Cartesian coordinate system $Oxyz$ is applied to describe the wave scattering problem with $z = 0$ at the mean water surface and Oz pointing upwards. Here, N local cylindrical coordinate systems $O_n r_n \theta_n z$ for $n = 1, 2, 3, \ldots, N$ are also introduced corresponding to the nth plate (see figure 1*b*). In addition, one more cylindrical coordinate system $Or_0\theta_0 z$ (not plotted in figure 1) is defined with its origin coinciding with the Cartesian coordinate system. The mean wetted surface of the nth plate is denoted by Ω_n.

An array of circular porous elastic plates are set in motion by a plane incident wave. The water is assumed to be homogeneous, inviscid and incompressible, and its motion irrotational and time harmonic with a prescribed angular frequency ω. The velocity potential in the fluid domain can be expressed as $\mathrm{Re}[\phi(x, y, z)\,\mathrm{e}^{-\mathrm{i}\omega t}]$, where ϕ is the complex spatial velocity potential, i denotes the imaginary unit and t is the time.

The spatial velocity potential ϕ is a solution of the governing equations

$$(\partial_x^2 + \partial_y^2 + \partial_z^2)\phi = 0 \quad \text{in the fluid domain} \tag{2.1}$$

with

$$\partial_z\phi = 0, \quad \text{on } z = -h \tag{2.2}$$

and

$$-\omega^2\phi + g\partial_z\phi = 0, \quad \text{on } z = 0 \tag{2.3}$$

at the water surface of the exterior region.

The floating porous elastic plate is modelled as a thin plate of constant thickness and shallow draft, which is assumed to be in contact with the water at all times following Meylan (2002). Kirchhoff–Love thin-plate theory, modified to include porosity, is used to model the plate motions. The velocity potential is coupled to the plate displacement function via kinematic and dynamic conditions, respectively,

$$\partial_z\phi = -\mathrm{i}\omega\eta^{(n)} + \mathrm{i}c\phi, \quad g[\chi\Delta^2 + 1 - (\omega^2/g)\gamma]\eta^{(n)} - \mathrm{i}\omega\phi = 0, \quad \text{for } \Omega_n, \tag{2.4a,b}$$

where $\eta^{(n)}$ denotes the complex vertical displacement of the lower surface of the nth plate; g represents the acceleration of gravity; $c = \omega K\rho/(\mu h)$ denotes the porosity parameter, in which K represents the permeability of the plate, ρ and μ are the density and dynamic
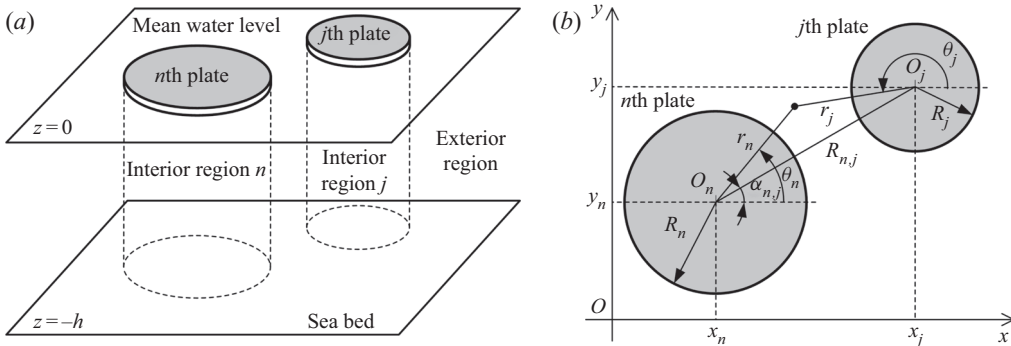
FIGURE 1. Schematic of an array of circular floating porous elastic plates: (*a*) side view; (*b*) plan view.

viscosity of water, respectively; γ and χ denote the mass per unit area and the flexural rigidity of the plate, respectively, scaled with respect to the water density; Δ is the Laplacian operator in the horizontal plane. With the employment of the Laplace equation as given in (2.1), the kinematic and dynamic conditions as given in (2.4*a*,*b*) can be combined into

$$(\omega^2/g)\phi = [\chi \partial_z^4 + 1 - (\omega^2/g)\gamma](\partial_z - ic)\phi. \tag{2.5}$$

Additionally, in the far-field horizontally, the scattered wave potential, $\phi_S = \phi - \phi_I$, where ϕ_I is the velocity potential of the undisturbed incident waves whose expression will be given in § 3, is subject to the Sommerfeld radiation condition.

The boundary conditions at the edge of each plate should be satisfied as well, which are dependent on the type of plate edge. In this paper, three different edge types, i.e. a clamped edge, a simply supported edge and a free edge, are considered.

For a clamped edge, both displacement and slope vanish at the edge, providing

$$\eta^{(n)} = 0 \quad \text{and} \quad \partial_n \eta^{(n)} = 0, \tag{2.6a,b}$$

where $\eta^{(n)}$ can be expressed in terms of ϕ by using the first component of (2.4*a*,*b*) and ∂_n represents the derivative operator corresponding to the normal vector on the edge $\vec{n} = (\cos\alpha_n, \sin\alpha_n)$, in which α_n is a function of the parameter s defining locations on the boundary of the nth plate (Meylan *et al.* 2017).

For a simply supported edge, both displacement and moment vanish at the edge, providing

$$\eta^{(n)} = 0 \quad \text{and} \quad F_M^{(n)} = 0, \tag{2.7a,b}$$

where

$$F_M^{(n)} = \Delta\eta^{(n)} - (1-\upsilon)\left(\partial_s^2\eta^{(n)} + \frac{d\alpha_n}{ds}\partial_n\eta^{(n)}\right) = \frac{\partial^2\eta^{(n)}}{\partial r_n^2} + \frac{\upsilon}{R_n^2}\frac{\partial^2\eta^{(n)}}{\partial\theta_n^2} + \frac{\upsilon}{R_n}\frac{\partial\eta^{(n)}}{\partial r_n}, \tag{2.8}$$

in which υ denotes the Poisson ratio, ∂_s represents the derivative operator corresponding to the tangential vector on the plate edge $\vec{s} = (-\sin\alpha_n, \cos\alpha_n)$.

For a free edge, both moment and shearing stress vanish at the edge, providing

$$F_M^{(n)} = 0 \quad \text{and} \quad F_V^{(n)} = 0, \tag{2.9a,b}$$

where

$$
\begin{aligned}
F_V^{(n)} &= \partial_n \Delta \eta^{(n)} + (1 - \upsilon) \partial_s \partial_n \partial_s \eta^{(n)} \\
&= \frac{\partial^3 \eta^{(n)}}{\partial r_n^3} + \frac{(2 - \upsilon)}{R_n^2} \frac{\partial^3 \eta^{(n)}}{\partial r_n \partial \theta_n^2} + \frac{1}{R_n} \frac{\partial^2 \eta^{(n)}}{\partial r_n^2} - \frac{(3 - \upsilon)}{R_n^3} \frac{\partial^2 \eta^{(n)}}{\partial \theta_n^2} - \frac{1}{R_n^2} \frac{\partial \eta^{(n)}}{\partial r_n}.
\end{aligned}
\tag{2.10}
$$

3. Theoretical solution to velocity potentials

The velocity potentials in the exterior region and interior region beneath the nth plate are denoted by ϕ_{ext} and $\phi_{int}^{(n)}$, respectively. Expressions for them are given as follows.

3.1. *Exterior region*

Here

$$\phi_{ext} = \phi_I + \sum_{n=1}^{N} \sum_{m=-\infty}^{\infty} \sum_{l=0}^{\infty} A_{m,l}^{(n)} H_m(k_l r_n) Z_l(z) \, \mathrm{e}^{\mathrm{i}m\theta_n}, \tag{3.1}$$

where the accumulative term denotes the scattered wave potential, ϕ_S; $A_{m,l}^{(n)}$ are the unknown coefficients to be determined; $Z_l(z) = \cosh[k_l(z + h)]/\cosh(k_l h)$; $k_0 \in \mathbb{R}^+$ and $k_l \in \mathrm{i}\mathbb{R}^+$ for $l = 1, 2, 3, \ldots$ support the propagating waves and evanescent waves, respectively, and they are the positive real root and the infinite positive imaginary roots of the dispersion relation for the exterior region

$$\omega^2 = g k_l \tanh(k_l h); \tag{3.2}$$

H_m is the Hankel function of the first kind of the mth order; ϕ_I denotes the undisturbed incident wave velocity potential, which can be expressed as

$$\phi_I(x, y, z) = -\frac{\mathrm{i}gA}{\omega} Z_0(z) \, \mathrm{e}^{\mathrm{i}k(x \cos \beta + y \sin \beta)}, \tag{3.3a}$$

$$\phi_I(r_n, \theta_n, z) = -\frac{\mathrm{i}gA}{\omega} Z_0(z) \, \mathrm{e}^{\mathrm{i}k(x_n \cos \beta + y_n \sin \beta)} \sum_{m=-\infty}^{\infty} \mathrm{i}^m \, \mathrm{e}^{-\mathrm{i}m\beta} J_m(kr_n) \, \mathrm{e}^{\mathrm{i}m\theta_n}, \tag{3.3b}$$

where (3.3a) and (3.3b) are written in the general Cartesian coordinate system $Oxyz$ and the local cylindrical coordinate systems $O_n r_n \theta_n z$, respectively, in which J_m denotes the Bessel function of the mth order. The second term on the right-hand side of (3.1), i.e. the accumulation term, represents the scattered wave potential, $\phi_S = \phi - \phi_I$, as mentioned in § 2, which is subject to the Sommerfeld radiation condition.

After using Graf's addition theorem for Bessel functions (Abramowitz & Stegun 1972; Zheng, Zhang & Iglesias 2018; Zheng *et al.* 2019), (3.1) can be rewritten in the cylindrical

coordinates $O_n r_n \theta_n z$ as

$$
\phi_{ext}(r_n, \theta_n, z) = \phi_I + \sum_{m=-\infty}^{\infty} \sum_{l=0}^{\infty} A_{m,l}^{(n)} H_m(k_l r_n) Z_l(z) \, e^{im\theta_n}
$$

$$
+ \sum_{\substack{j=1, \ m=-\infty \\ j \neq n}}^{N} \sum_{l=0}^{\infty} A_{m,l}^{(j)} Z_l(z) \sum_{m'=-\infty}^{\infty} (-1)^{m'} H_{m-m'}(k_l R_{n,j}) J_{m'}(k_l r_n)
$$

$$
\times \, e^{i(m\alpha_{j,n} - m'\alpha_{n,j})} \, e^{im'\theta_n} \quad \text{for } r_n < \min_{\substack{j=1,N; \\ j \neq n}} R_{n,j}. \tag{3.4}
$$

3.2. *Interior region*

Here

$$
\phi_{int}^{(n)}(r_n, \theta_n, z) = \sum_{m=-\infty}^{\infty} \sum_{l=-2}^{\infty} B_{m,l}^{(n)} J_m(\kappa_l r_n) Y_l(z) \, e^{im\theta_n}, \tag{3.5}
$$

where $B_{m,l}^{(n)}$ are the unknown coefficients to be determined; $Y_l = \cosh[\kappa_l(z+h)]/\cosh(\kappa_l h)$; κ_l for $l = -2, -1, 0, 1, 2, \ldots$ are the roots of the dispersion relation for the interior region

$$
[\chi \kappa_l^4 + 1 - (\omega^2/g)\gamma][\kappa_l \tanh(\kappa_l h) - ic] = \omega^2/g. \tag{3.6}
$$

For $c = 0$, $\kappa_0 \in \mathbb{R}^+$ and $\kappa_l \in i\mathbb{R}^+$ for $l = 1, 2, 3, \ldots$ can be obtained, which support the propagating waves and evanescent waves, respectively. The remaining two roots, κ_{-2} and κ_{-1}, support damped propagating waves, and satisfy $\kappa_{-1} \in \mathbb{R}^+ + i\mathbb{R}^+$ and $\kappa_{-2} = -\kappa_{-1}^*$, in which * denotes the complex conjugate. For $c \neq 0$, the structure of κ_l is perturbed. In general, neither pure real nor pure imaginary roots exist, and the symmetry between κ_{-2} and κ_{-1} is not valid either (Meylan *et al.* 2017). The method to compute them efficiently is given in Meylan *et al.* (2017) and Zheng *et al.* (2020).

Note that the spatial velocity potentials as given in (3.4) and (3.5) already satisfy all the governing equation and boundary conditions as listed in § 2, except at the plate edges. In addition, continuity of pressure and the radial velocity at the interfaces between the exterior region and interior regions should also be satisfied. These continuity conditions can be expressed as follows.

(i) Continuity of pressure at the boundary $r_n = R_n$:

$$
\phi_{ext}\big|_{r_n = R_n} = \phi_{int}^{(n)}\big|_{r_n = R_n}, \quad -h < z < 0. \tag{3.7}
$$

(ii) Continuity of radial velocity at the boundary $r_n = R_n$:

$$
\frac{\partial \phi_{ext}}{\partial r_n}\bigg|_{r_n = R_n} = \frac{\partial \phi_{int}^{(n)}}{\partial r_n}\bigg|_{r_n = R_n}, \quad -h < z < 0. \tag{3.8}
$$

The continuity conditions, i.e. (3.7)–(3.8), together with the edge type dependent edge conditions, i.e. (2.6*a,b*), (2.7*a,b*) or (2.9*a,b*), can be used to derive a complex linear matrix equation by using the orthogonality characteristics of $Z_l(z)$ and $e^{im\theta_n}$, and the eigenfunction-matching method. The unknown coefficients $A_{m,l}^{(n)}$ and $B_{m,l}^{(n)}$ can then be calculated by solving the complex linear matrix equation. Detailed derivation and calculations for the unknown coefficients are given in appendix A.

4. Far-field coefficients, Kochin functions and wave-power dissipation

We present here two derivations of the wave-power dissipation due to the porosity.

4.1. *Wave-power dissipation: direct method*

The energy dissipated by the N plates due to the porosity, P_{diss}, can be calculated by

$$
P_{diss} = \frac{c}{2\rho\omega} \sum_{n=1}^{N} \iint_{\Omega_n} |p|^2 \, \mathrm{d}s = \frac{\rho\omega c}{2} \sum_{n=1}^{N} \iint_{\Omega_n} |\phi|^2 \, \mathrm{d}s
$$

$$
= \frac{\rho\omega c}{2} \sum_{n=1}^{N} \iint_{\Omega_n} \left| \sum_{m=-\infty}^{\infty} \sum_{l=-2}^{\infty} B_{m,l}^{(n)} J_m(\kappa_l r_n) \, \mathrm{e}^{\mathrm{i}m\theta_n} \right|^2 \mathrm{d}s, \tag{4.1}
$$

where p denotes the hydrodynamic pressure under the plates, $p = \mathrm{i}\omega\rho\phi$.

The dimensionless quantity of P_{diss} can be defined by

$$
\eta_{diss} = kP_{diss}/P_{in}, \tag{4.2}
$$

in which P_{in} is the incoming wave power per unit width of the wave front given by

$$
P_{in} = \frac{\rho g A^2}{2} \frac{\omega}{2k} \left(1 + \frac{2kh}{\sinh(2kh)} \right). \tag{4.3}
$$

4.2. *Wave-power dissipation: indirect method*

We present here another, more general, derivation of the power dissipation identity. In this expression, we use the very general equations of motion which govern a floating elastic plate of arbitrary geometry.

Firstly, let us consider the far-field coefficients and Kochin functions. In the fluid domain, far away from an array of porous elastic plates, only the propagating modes exist in the scattered waves. With the asymptotic forms of H_m for $r_0 \to \infty$,

$$
H_m(kr_0) = \sqrt{2/\pi}\mathrm{e}^{-\mathrm{i}(m\pi/2+\pi/4)}(kr_0)^{-1/2}\,\mathrm{e}^{\mathrm{i}kr_0} \quad \text{for } r_0 \to \infty, \tag{4.4}
$$

where k is employed to represent k_0 for simplification, the scattered wave potential, i.e. the accumulative term in (3.1), can be rewritten as

$$
\phi_S = \sqrt{2/\pi}Z_0(z) \sum_{n=1}^{N} \sum_{m=-\infty}^{\infty} A_{m,0}^{(n)} \mathrm{e}^{-\mathrm{i}(m\pi/2+\pi/4)}(kr_n)^{-1/2}\,\mathrm{e}^{\mathrm{i}kr_n}\,\mathrm{e}^{\mathrm{i}m\theta_n}, \quad r_0 \to \infty, \tag{4.5}
$$

which can be further expressed in the global polar coordinate system $O_0 r_0 \theta_0 z$ as

$$
\phi_S = \sqrt{2/\pi}(kr_0)^{-1/2}\,\mathrm{e}^{\mathrm{i}kr_0} Z_0(z) \sum_{n=1}^{N} \sum_{m=-\infty}^{\infty} A_{m,0}^{(n)} \mathrm{e}^{-\mathrm{i}kR_{0,n}\cos(\alpha_{0,n}-\theta_0)}\,\mathrm{e}^{-\mathrm{i}(m\pi/2+\pi/4)}\,\mathrm{e}^{\mathrm{i}m\theta_0}
$$

$$
= A_R(\theta_0)(kr_0)^{-1/2}\,\mathrm{e}^{\mathrm{i}kr_0} Z_0(z), \quad r_0 \to \infty, \tag{4.6}
$$

where A_R is the so-called far-field coefficient that is independent of r_0 and z, and can be expressed as

$$A_R(\theta_0) = \sqrt{2/\pi} \sum_{n=1}^{N} \sum_{m=-\infty}^{\infty} A_{m,0}^{(n)} e^{-ikR_{0,n}\cos(\alpha_{0,n}-\theta_0)} e^{-i(m\pi/2+\pi/4)} e^{im\theta_0}. \tag{4.7}$$

The Kochin function, H_R, which is a scale version of the far-field coefficient, can be obtained from A_R as follows (Falnes 2002):

$$H_R(\theta_0) = \sqrt{2\pi} \, e^{-i\pi/4} A_R(\theta_0)$$
$$= 2 \sum_{n=1}^{N} \sum_{m=-\infty}^{\infty} A_{m,0}^{(n)} e^{-ikR_{0,n}\cos(\alpha_{0,n}-\theta_0)} (-i)^{m+1} e^{im\theta_0}. \tag{4.8}$$

In the water domain enclosed by $\Omega_1 \cup \Omega_2 \cup \cdots \cup \Omega_N \cup \Omega_R$, free water surface and the sea bed, using Green's theorem (Falnes 2002; Fàbregas Flavià & Meylan 2019), we have

$$\oiint \left(\phi \frac{\partial \phi^*}{\partial n} - \phi^* \frac{\partial \phi}{\partial n} \right) ds$$
$$= \sum_{n=1}^{N} \iint_{\Omega_n} \left(\phi \frac{\partial \phi^*}{\partial z} - \phi^* \frac{\partial \phi}{\partial z} \right) ds + \iint_{\Omega_R} \left(\phi \frac{\partial \phi^*}{\partial r} - \phi^* \frac{\partial \phi}{\partial r} \right) ds = 0, \tag{4.9}$$

where Ω_R represents an envisaged vertical cylindrical control surface with its radius denoted by $r_0 = R_0$, which is large enough to enclose all the plates.

With utilisation of the first component of (2.4a,b), (4.9) can be rewritten as

$$\sum_{n=1}^{N} \iint_{\Omega_n} \left[i\omega \left(\phi \eta^{(n)*} + \phi^* \eta^{(n)} \right) - 2ic|\phi|^2 \right] ds + \iint_{\Omega_R} \left(\phi \frac{\partial \phi^*}{\partial r} - \phi^* \frac{\partial \phi}{\partial r} \right) ds = 0. \tag{4.10}$$

We are setting out to show that the accumulation of the terms within the first parentheses in (4.10) vanishes.

The response of the nth plate can be expressed by a series of natural modes of vibration of the plate *in vacuo* as (Meylan *et al.* 2017)

$$\eta^{(n)} \approx \sum_{q=1}^{Q} u_q^{(n)} \eta_q^{(n)}, \tag{4.11}$$

where the modes $\eta_q^{(n)}$ satisfy the eigenvalue problem for the biharmonic operator

$$\Delta^2 \eta_q^{(n)} = \lambda_q \eta_q^{(n)}, \tag{4.12}$$

together with the edge conditions as given in § 2; $\eta_q^{(n)}$ are orthogonal for different eigenvalues λ_q, and Q denotes the truncated numbers of the infinite modes.

The dynamic motion of the plates can be coupled with the hydrodynamics by

$$\left(\boldsymbol{K} + \boldsymbol{C} - \frac{\omega^2}{g} \boldsymbol{M} \right) \boldsymbol{u} = \mathrm{i}\omega\rho \iint_{\Omega_{sum}} \phi \boldsymbol{n} \, \mathrm{d}s, \tag{4.13}$$

where $\Omega_{sum} = \Omega_1 \cup \Omega_2 \cup \cdots \cup \Omega_N$, $\boldsymbol{K}$, $\boldsymbol{C}$ and $\boldsymbol{M}$ are $(NQ) \times (NQ)$ square matrices that represent stiffness, hydrostatic-restoring and mass matrices, respectively,

$$\boldsymbol{K} = \left\langle \chi \lambda_q \right\rangle_{(n-1)Q+q} ; \quad \boldsymbol{C} = \boldsymbol{I}; \quad \boldsymbol{M} = \gamma \boldsymbol{I}, \tag{4.14a-c}$$

in which $\langle c_i \rangle_j$ denotes a diagonal matrix with diagonal entries c_i at the position (j, j), $\boldsymbol{I}$ is the identity matrix and

$$\boldsymbol{u} = \left[u_q^{(n)} \right]_{(n-1)Q+q}, \quad \boldsymbol{n} = \left[\eta_q^{(n)} \right]_{(n-1)Q+q}, \tag{4.15a,b}$$

where $[c_i]_j$ represents a vector with entries c_i at the jth row.

With the employment of (4.11) and (4.13), it can be proved that

$$\sum_{n=1}^{N} \iint_{\Omega_n} \left(\phi \eta^{(n)*} + \phi^* \eta^{(n)} \right) \mathrm{d}s = \sum_{n=1}^{N} \iint_{\Omega_n} \left(\phi \sum_{q=1}^{Q} u_q^{(n)*} \eta_q^{(n)} + \phi^* \sum_{q=1}^{Q} u_q^{(n)} \eta_q^{(n)} \right) \mathrm{d}s$$

$$= \iint_{\Omega_{sum}} \left\{ -\phi(\boldsymbol{x}) \left[\left(\boldsymbol{K} + \boldsymbol{C} - \frac{\omega^2}{g} \boldsymbol{M} \right)^{-1} \mathrm{i}\omega\rho \iint_{\Omega_{sum}} \phi^*(\bar{\boldsymbol{x}}) \boldsymbol{n}(\bar{\boldsymbol{x}}) \, \mathrm{d}\bar{s} \right]^{\mathrm{T}} \boldsymbol{n}(\boldsymbol{x}) \right.$$

$$\left. +\phi^*(\boldsymbol{x}) \left[\left(\boldsymbol{K} + \boldsymbol{C} - \frac{\omega^2}{g} \boldsymbol{M} \right)^{-1} \mathrm{i}\omega\rho \iint_{\Omega_{sum}} \phi(\bar{\boldsymbol{x}}) \boldsymbol{n}(\bar{\boldsymbol{x}}) \, \mathrm{d}\bar{s} \right]^{\mathrm{T}} \boldsymbol{n}(\boldsymbol{x}) \right\} \mathrm{d}s$$

$$= 0, \tag{4.16}$$

where we used the symmetry of the matrix $(\boldsymbol{K} + \boldsymbol{C} - (\omega^2/g)\boldsymbol{M})^{-1}$ and reversed the order of integration.

Therefore, (4.10) reads

$$\sum_{n=1}^{N} \iint_{\Omega_n} \left(-2\mathrm{i}c|\phi|^2 \right) \mathrm{d}s + \iint_{\Omega_R} \left(\phi \frac{\partial \phi^*}{\partial r} - \phi^* \frac{\partial \phi}{\partial r} \right) \mathrm{d}s = 0, \tag{4.17}$$

hence the power dissipation can be expressed as

$$P_{diss} = \frac{\rho\omega c}{2} \sum_{n=1}^{N} \iint_{\Omega_n} |\phi|^2 \, \mathrm{d}s = \frac{\rho\omega}{4\mathrm{i}} \iint_{\Omega_R} \left(\phi \frac{\partial \phi^*}{\partial r} - \phi^* \frac{\partial \phi}{\partial r} \right) \mathrm{d}s, \tag{4.18}$$

which, from the view of energy identities, presents an approach to evaluate the power dissipation based on the spatial potentials in the exterior region.

When $r_0 = R_0 \to \infty$, (4.18) holds as well with the control surface Ω_R replaced by Ω_∞, i.e. $r_0 \to \infty$. An expression for the integral in (4.18) in terms of Kochin functions (Falnes 2002) is

$$\iint_{\Omega_\infty} \left(\phi \frac{\partial \phi^*}{\partial r_0} - \phi^* \frac{\partial \phi}{\partial r_0} \right) \mathrm{d}s = \frac{2\mathrm{i}AgD(kh)}{\omega k} \mathrm{Re}[H_R(\beta)] - \frac{\mathrm{i}D(kh)}{2\pi k} \int_0^{2\pi} |H_R(\theta_0)|^2 \, \mathrm{d}\theta_0,$$

(4.19)

where

$$D(kh) = \left[1 + \frac{2kh}{\sinh(2kh)} \right] \tanh(kh).$$

(4.20)

Therefore, the power dissipated by the array of porous elastic plates can be evaluated by using an indirect method based on Kochin functions

$$P_{diss} = \frac{\rho \omega D(kh)}{k} \left(\frac{Ag}{2\omega} \mathrm{Re}[H_R(\beta)] - \frac{1}{8\pi} \int_0^{2\pi} |H_R(\theta_0)|^2 \, \mathrm{d}\theta_0 \right).$$

(4.21)

Compared with the straightforward method, i.e. (4.1), which includes the surface integrals over all the plates with both propagating and evanescent waves considered, the indirect method as given in (4.21) consists of only one angular integral regardless of the number of plates, and uses the propagating waves only to achieve an accurate evaluation of the wave-power dissipation. Moreover, (4.21) is derived without any employment of the 'circular-shape' restriction, therefore the indirect method applies to the floating porous elastic plates with non-circular shapes as well. Finally, the existence of two different identities gives a method to check the accuracy of the numerical solution, in much the same way that energy conservation can be used in the case of a floating body which does not dissipate energy.

5. Validation

If the spacing between the porous elastic plates is large, the hydrodynamic interaction between them can be neglected. Therefore the response of every plate will be close to that of the plate in isolation. Figure 2 presents the comparison of the displacements of a circular porous elastic plate in isolation (Meylan *et al.* 2017) and a pair of the same plates arranged far away from one another, where c, χ and γ are non-dimensionalised with respect to the water depth as $\bar{c} = ch$, $\bar{\chi} = \chi/h^4$ and $\bar{\gamma} = \gamma/h$, respectively. Additionally, the energy dissipated due to porosity as a function of $\bar{c}/N$ is provided in figure 3, where E is a quantity proportional to the wave-energy dissipated due to the porosity, which was calculated by integrating the far-field amplitude functions based on a coupled boundary-element and finite element method (Meylan *et al.* 2017). The present results agree well with those of Meylan *et al.* (2017) and Zheng *et al.* (2020).

We have also compared our model with the experimental data in the case of non-porous plates. Montiel *et al.* (2013*a*) carried out a series of wave basin experiments on a pair of circular floating elastic plates and observed strong hydrodynamic interaction between them. One of the cases tested by Montiel *et al.* (2013*a*), is plotted in figure 4, where four motion tracking markers were placed on each plate. Figure 5 illustrates the theoretical and experimental deflection of the four markers for the two plates. The results show that the present conceptual model can be used to predict the response of the two elastic plates accurately and that it provides insights into the interaction between the two plates.
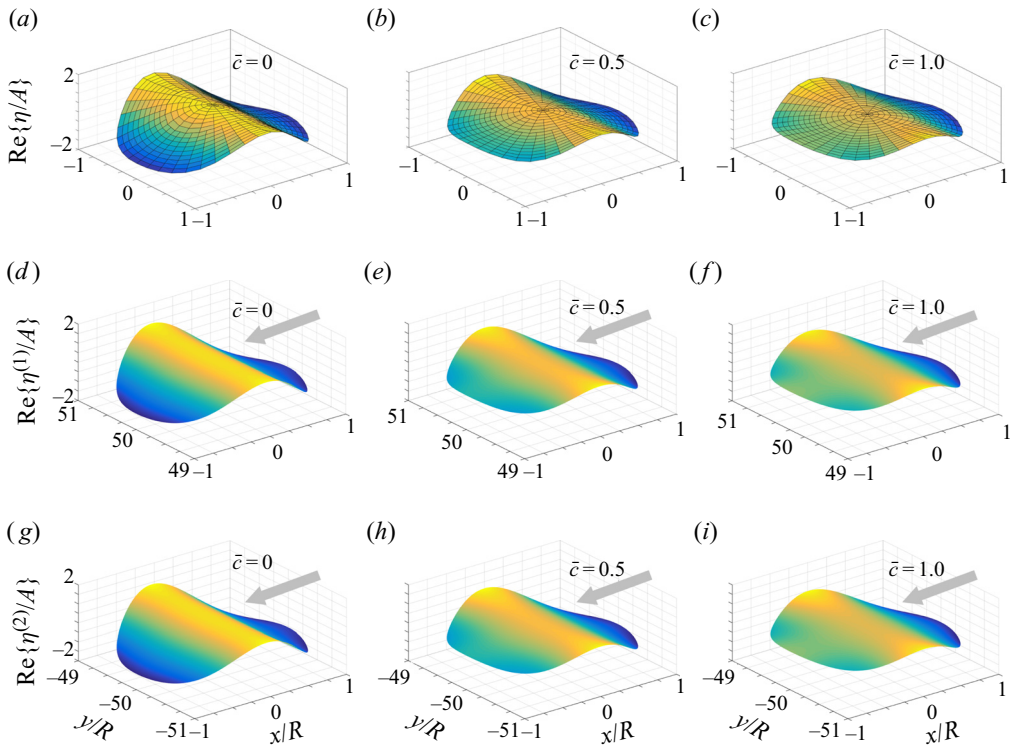
FIGURE 2. (*a–c*) Displacements of a circular plate in isolation (Meylan *et al.* 2017), where a typo of the incident wave direction existed (i.e. β was typed as 0 rather than π); (*d–f*) and (*g–i*) displacements of plate-1 and plate-2 in a pair of plates (present results) at $t = 0$ for different porosity parameter $\bar{c} = 0, 0.5$ and 1.0. ($R_1 = R_2 = R$, $x_1 = x_2 = 0$, $y_1/R = -y_2/R = 50$, $R/h = 2.0$, $\beta = \pi$, $h\omega^2/g = 2.0$ and $\bar{\chi} = \bar{\gamma} = 0.01$, free edge.)
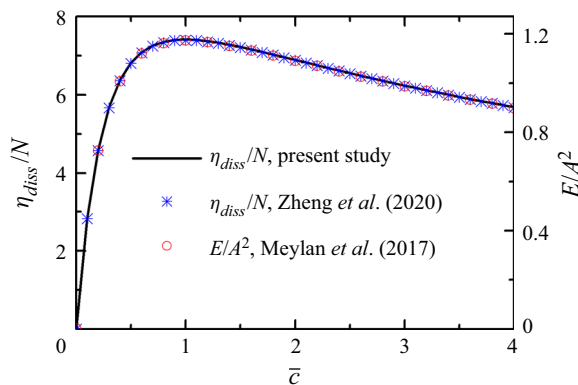

FIGURE 3. Wave-power dissipation by floating circular plates with a free edge versus the porosity parameter for $R/h = 2.0$, $\beta = \pi$, $h\omega^2/g = 2.0$ and $\bar{\chi} = \bar{\gamma} = 0.01$ (lines: present results with $N = 2$, $R_1 = R_2 = R$, $x_1 = x_2 = 0$, $y_1/R = -y_2/R = 50$; symbols: Zheng *et al.* (2020) and Meylan *et al.* (2017) with $N = 1$).
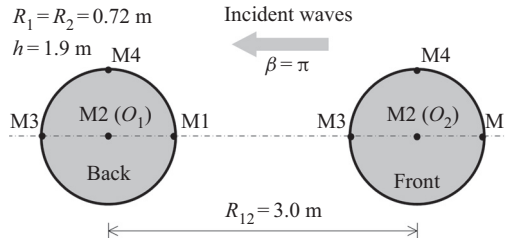
FIGURE 4. Deployment of two circular elastic plates. Four markers are labelled in each plate for reference. ($\bar{c} = 0$, $\bar{\chi} = 3.55 \times 10^{-4}$, $\bar{\gamma} = 2.79 \times 10^{-3}$, free edge.)
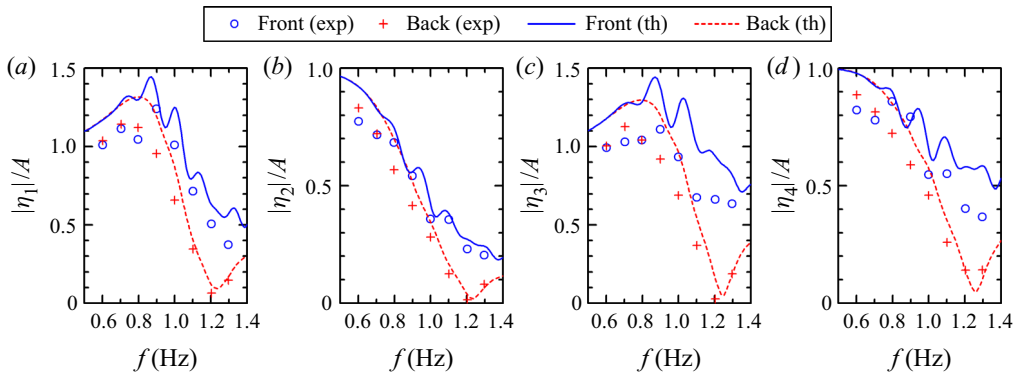

FIGURE 5. Deflection of (*a*) marker 1; (*b*) marker 2; (*c*) marker 3 and (*d*) marker 4 for the two-plate arrangement as given in figure 4, as a function of frequency. Each figure contains the present theoretical results and the experimental data (Montiel *et al.* 2013*a*) associated with both plates. ($\bar{c} = 0$, $\bar{\chi} = 3.55 \times 10^{-4}$, $\bar{\gamma} = 2.79 \times 10^{-3}$, free edge.)
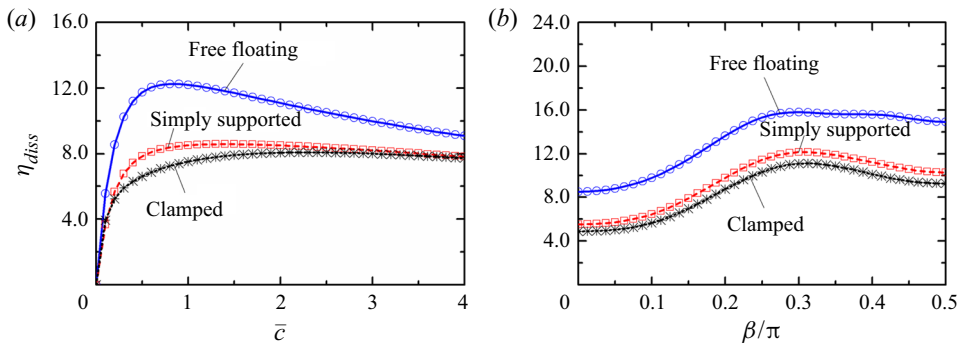
FIGURE 6. Wave-power dissipation of two plates with different edge conditions evaluated by using direct method (lines) and indirect method (symbols): (*a*) variation of η_{diss} with $\bar{c}$ for $\beta = \pi/6$; (*b*) variation of η_{diss} with β for $\bar{c} = 1.0$. ($N = 2$, $-x_1/h = x_2/h = 3.0$, $y_1 = y_2 = 0$, $R/h = 2.0$, $h\omega^2/g = 2.0$, $\bar{\chi} = \bar{\gamma} = 0.01$.)

In addition to the comparison of the present theoretical results with the published data, wave-power dissipation by two porous elastic plates is evaluated by using both direct and indirect methods (figure 6). The excellent agreement of the results (figure 6), together with those plotted in figures 2, 3 and 5 gives clear validation of the present theoretical model
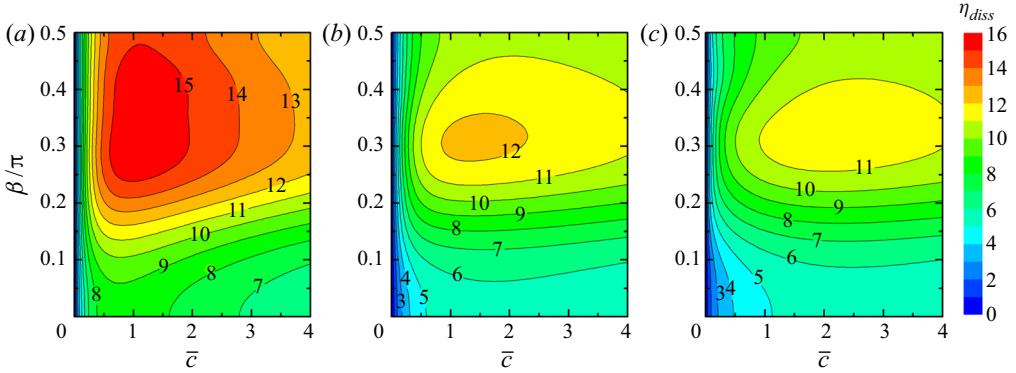
FIGURE 7. Contour plot for the variation of η_{diss} as a function of porosity parameter $\bar{c}$ and incident wave direction β: (*a*) free edge; (*b*) simply supported edge; (*c*) clamped edge. ($N = 2$, $-x_1/h = x_2/h = 3.0$, $y_1 = y_2 = 0$, $R/h = 2$, $h\omega^2/g = 2.0$, $\bar{\chi} = \bar{\gamma} = 0.01$.)

for solving wave scattering and evaluating wave dissipation by an array of circular floating porous elastic plates.

6. Results and discussion

6.1. *Effect of porosity and incident wave direction*

The response of an array of circular floating porous elastic plates and their performance in terms of wave-power dissipation are strongly affected by both the porosity, $\bar{c}$, and the incident wave direction, β. In this subsection, a pair of plates deployed along the x-axis with $R/h = 2.0$, $R_{1,2}/h = 6.0$, $\bar{\chi} = \bar{\gamma} = 0.01$ and $h\omega^2/g = 2.0$ is taken as an example to examine the influence of $\bar{c}$ and β. Figure 7 presents how η_{diss} varies with the incident wave direction β and also with the porosity parameter $\bar{c}$ for the cases with free edges, simply supported edges and clamped edges.

When $\bar{c} \to 0$, the plates become non-porous and no power will be dissipated. When $\bar{c} \to \infty$, on the other hand, there is no resistance to flow by the plate, and in this limit, there is also no dissipation of power. For this reason, there exists an optimal porosity parameter $\bar{c}$ to maximise the dissipated wave power. As shown in figure 7, for any given wave incident direction, the more strictly the plate edge is constrained, the larger the optimal $\bar{c}$ for maximising wave-power dissipation. Although η_{diss} varies dramatically with the change of $\bar{c}$ for $\bar{c} < 0.5$ for all the three cases, it becomes less sensitive to $\bar{c}$ for $1.0 < \bar{c} < 4.0$ compared with $\bar{c} < 1.0$, especially for the simply supported and clamped edge cases.

For the pair of plates with a fixed porosity, the wave-power dissipated is minimum when incident waves propagate along the two plates, i.e. $\beta = 0$. This minimal case results from the significant reduction of the wave power dissipated by the leeward plate due to the 'shadowing effect' of the wave-ward plate. For $R_{1,2}/h = 6.0$, as β increases from 0 towards $\pi/2$, η_{diss} first increases and then decreases after reaching its peak value, regardless of the types of edge conditions. The wave incident direction corresponding to the maximum wave-power dissipation, as illustrated in figure 7 remains around $\beta/\pi = 0.3$ for all three cases. The largest wave-power dissipation in terms of η_{diss} for these cases are 15.79, 12.24 and 11.63, occurring at $(\bar{c}, \beta/\pi) = (1.05, 0.30)$, $(1.35, 0.31)$ and $(2.10, 0.32)$, respectively.
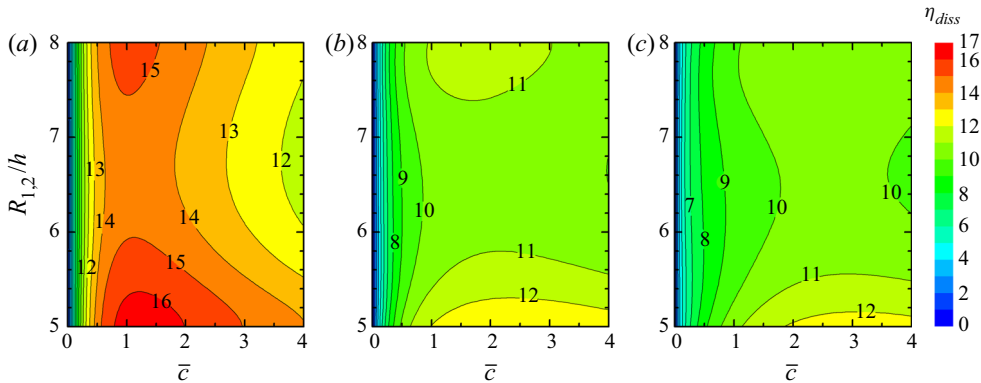
FIGURE 8. Contour plot for the variation of η_{diss} as a function of porosity parameter $\bar{c}$ and distance between the centres of the plates $R_{1,2}$: (*a*) free edge; (*b*) simply supported edge; (*c*) clamped edge. ($N = 2$, $-x_1/h = x_2/h = 0.5R_{1,2}/h$, $y_1 = y_2 = 0$, $R/h = 2.0$, $h\omega^2/g = 2.0$, $\beta = \pi/2$, $\bar{\chi} = \bar{\gamma} = 0.01$.)

6.2. *Effect of the distance between the plate centres*

The distance between the plate centres is a pivotal parameter affecting the response and wave-power dissipation of an array of porous elastic plates. The two plates, as studied in § 6.1, with their centre distance $R_{1,2}/h$ ranging from 5.0 to 8.0, together with different porosity parameters in wave condition $h\omega^2/g = 2.0$, $\beta = \pi/2$, are examined in this section, the results of which are plotted in figure 8.

In the computed range of $\bar{c}$ and $R_{1,2}/h$ there are two peaks of η_{diss}, one occurring at $R_{1,2}/h = 5.0$ and the other at $R_{1,2}/h = 8.0$, in which the former one is higher than the aft one regardless of the types of plate edge condition. More specifically, the largest values of η_{diss} are 16.49, 12.79, 12.38, for the free, simply supported and clamped cases, occurring at $(\bar{c}, R_{1,2}/h)$=(1.25, 5.0), (2.25, 5.0) and (3.00, 5.0), respectively, which are caused by the hydrodynamic interaction between the plates – the so-called array effect. Different regimes of wave interaction with the pair of plates are obtained as the spacing changes. The second peak is an effect of constructive interference, which can be analysed from the infinite array problem (see e.g. Peter, Meylan & Linton 2006). As $R_{1,2}/h$ continues to increase until it is large enough, hydrodynamic interaction between the plates will be negligible, and each of the plates will ultimately work as a plate working in isolation (see § 5). Case studies will be carried out with the centre distance between two adjacent plates as $R_{j,j+1}/h = 5.0$ due to the corresponding larger wave-power dissipation compared with the other values of $R_{j,j+1}/h$.

6.3. *Effect of the number of plates*

Figure 9 presents the variation of the wave-power dissipation of a line array of porous elastic plates in terms of η_{diss}/N with the porosity parameter $\bar{c}$ for $h\omega^2/g = 2.0$, $\beta = \pi/2$ and $R_{j,j+1}/h = 5.0$.

For $\bar{c} < 0.25$, the curves of η_{diss}/N with different values of N nearly overlap with each other, denoting the negligible impact of the number of plates in the array on wave-power dissipation. This is a case of the long array behaviour (see e.g. Montiel, Squire & Bennetts 2015*b*) being well approximated by a small array. For the rest of the computed range of
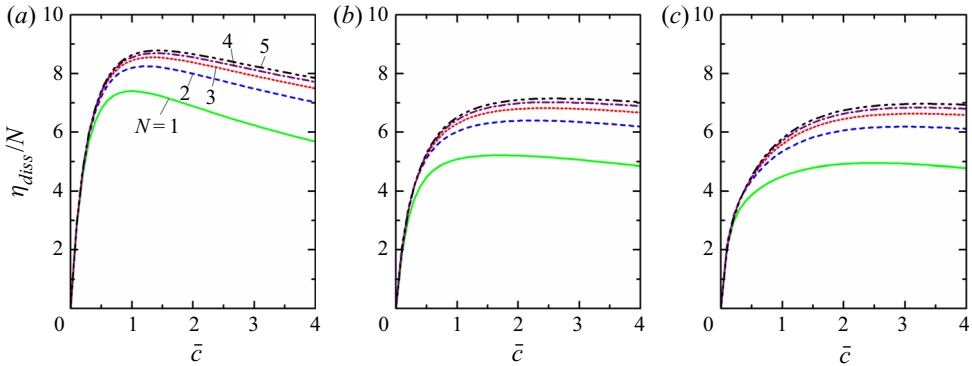
FIGURE 9. Variation of η_{diss}/N with porosity parameter $\bar{c}$ for different number of plates in the array, N: (*a*) free edge; (*b*) simply supported edge; (*c*) clamped edge. $((x_{j+1} - x_j)/h = 5.0$, $y_j = 0$, $R/h = 2.0$, $h\omega^2/g = 2.0$, $\beta = \pi/2$, $\bar{\chi} = \bar{\gamma} = 0.01$.)

Edge condition	$N = 1$	$N = 2$	$N = 3$	$N = 4$	$N = 5$
Free	(7.40, 1.0)	(8.25, 1.2)	(8.55, 1.3)	(8.69, 1.4)	(8.79, 1.4)
Simply supported	(5.21, 1.7)	(6.40, 2.2)	(6.82, 2.5)	(7.02, 2.6)	(7.15, 2.6)
Clamped	(4.95, 2.5)	(6.19, 3.0)	(6.63, 3.2)	(6.84, 3.2)	(6.97, 3.3)

TABLE 1. The peak value of wave-power dissipation and the corresponding optimal porosity parameter, $(\eta_{diss}/N, \bar{c})$, for the array consisting of different number of plates with different edge conditions. $((x_{j+1} - x_j)/h = 5.0$, $y_j = 0$, $R/h = 2.0$, $h\omega^2/g = 2.0$, $\beta = \pi/2$, $\bar{\chi} = \bar{\gamma} = 0.01$.)

$\bar{c}$, i.e. $\bar{c} > 0.25$, the $\eta_{diss}/N - \bar{c}$ curve rises with an increase of N. The most significant improvement of η_{diss}/N occurs when N increases from 1 to 2. For larger values of N, the increase in η_{diss}/N is weaker. This holds for all the edge conditions, i.e. free edges, simply supported edges and clamped edges, as plotted in figure 9. For instance, in the free-edge case with $\bar{c} = 1.0$, the η_{diss}/N corresponding to $N = 1 \sim 5$ are 7.40, 8.19, 8.45, 8.56 and 8.63, with the increasing percentage 10.7%, 3.1%, 1.3% and 0.9%, respectively. It can also be observed that the more plates the array contains, the larger the value of $\bar{c}$ required to achieve maximum wave-power dissipation. The peak value of η_{diss}/N and the corresponding optimal $\bar{c}$ for the array consisting of different numbers of plates with different edge conditions are listed in table 1.

Figure 10 presents the frequency response of the wave-power dissipation of an array of porous elastic plates in terms of η_{diss}/N for $\bar{c} = 1.0$, $\beta = \pi/2$. For the free-edge condition (figure 10*a*), the η_{diss}/N increases monotonically as kR increases from 0 towards 8.0 regardless of the plate numbers included in the array. While for the $N = 5$ cases with the simply supported and the clamped-edge conditions (figures 10*b* and 10*c*), a flat valley can be observed around $kR = 6.0$. As shown in figure 10, the array which contains more plates is found to lead to a larger value of η_{diss}/N for the whole computed range of wave conditions, except for the very long waves, e.g. $kR < 1.0$, where, on the contrary, the largest value of η_{diss}/N is obtained when $N = 1$. Similar to the results illustrated in figure 9, the frequency response of η_{diss}/N as given in figure 10 indicates that for most of the computed range of wave conditions, e.g. $kR > 1.5$, the most apparent increment of the wave-power dissipation in terms of η_{diss}/N is obtained when N increases from 1 to 2.
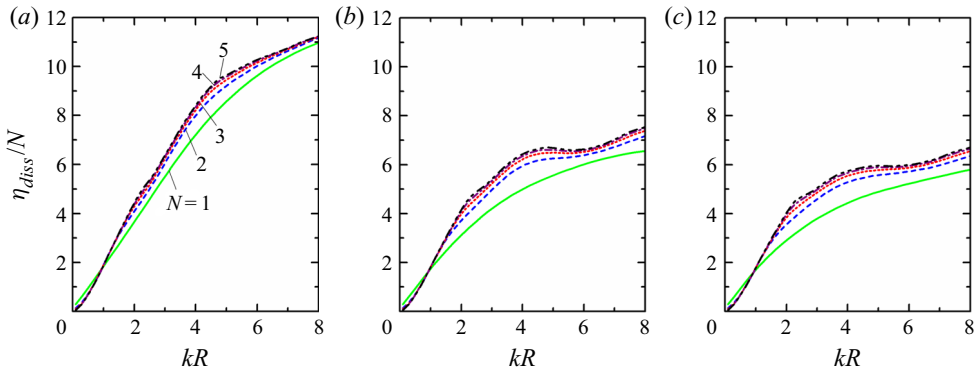
FIGURE 10. Variation of η_{diss}/N with wave number kR for different number of plates in the array, N: (*a*) free edge; (*b*) simply supported edge; (*c*) clamped edge. (($x_{j+1} - x_j)/h = 5.0$, $y_j = 0$, $R/h = 2.0$, $\bar{c} = 1.0$, $\beta = \pi/2$, $\bar{\chi} = \bar{\gamma} = 0.01$.)

The variation of η_{diss}/N with incident wave direction β in the range of $0 \leq \beta \leq 0.5\pi$ for different numbers of plates in the array, N, with $h\omega^2/g = 2.0$, $\bar{c} = 1.0$ is plotted in figure 11. As expected, the wave power dissipated by a single circular porous elastic plate, i.e. $N = 1$, is independent of β, regardless of the edge conditions. For the cases with $N \geq 2$, an overall growth of η_{diss}/N is observed as β increases from 0 to 0.5π. For β varying from a specified value, e.g. 0.29π for the free-edge condition, to 0.5π, the more plates included in the array, the larger the wave-power dissipation per plate, η_{diss}/N, becomes. Whereas when β is smaller than the specified value, the number of plates plays a negative role in the wave-power dissipation. It means that for the incident direction roughly perpendicular to the row of plates, the hydrodynamic interaction between the plates plays a constructive role in dissipating wave power. Moreover, this effect gets stronger as more plates are included in the array. However, if the incident waves propagate along the row of plates, a destructive effect of hydrodynamic interaction on wave-power dissipation is obtained, and the negative influence gets stronger correspondingly as the number of plates in the array increases. This is reasonable from the point of view of the shadow effect. The front plate creates a shadow, and the plates behind it do not respond as much. The more plates included in the array, the stronger the shadow effect for the plates at the back.

To demonstrate the effect of the number of plates on their response, the plate deflections for different edge conditions for various values of N with $\bar{c} = 1.0$, $h\omega^2/g = 2.0$, $\beta = \pi/2$ are plotted in figures 12–14. For the sake of simplicity, only the results of the first half of the plates in the array are displayed, including the middle one if N is odd.

As shown in figure 12, for the isolated single plate with free-edge condition, the largest deflection ($|\eta^{(n)}|_{max}/A = 0.93$) occurs at the front edge, i.e. the wave-ward edge. Moreover, there is an internal region near the leeward edge, where the response is weaker than the other regions of the plate, with the smallest deflection $|\eta^{(n)}|_{min}/A = 0.02$. When another plate with the same physical properties is placed nearby (i.e. $N = 2$), the weak response internal region shifts towards the array side slightly. The largest and smallest deflection (i.e. $|\eta^{(n)}|_{max}/A = 0.99$ and $|\eta^{(n)}|_{min}/A = 0.03$) are both larger than those for $N = 1$. What is more, apart from the largest deflection at the front edge, there is a second peak response ($|\eta^{(n)}|/A = 0.78$) observed at the edge close to the other plate, which is excited by the hydrodynamic interaction between them and contributes to the increase of η_{diss}/N. For the three-plate array, the side plates response is similar to those of the array with $N = 2$.
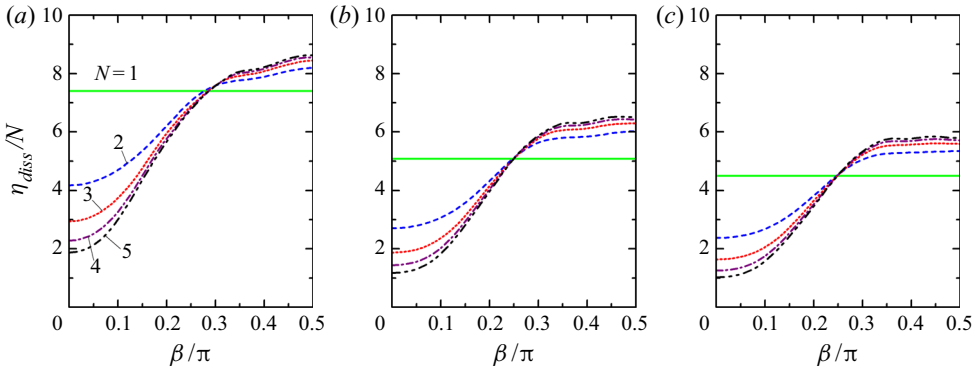
FIGURE 11. Variation of η_{diss}/N with incident wave direction β for different number of plates in the array, N: (a) free edge; (b) simply supported edge; (c) clamped edge. (($x_{j+1} - x_j)/h = 5.0$, $y_j = 0$, $R/h = 2.0$, $\bar{c} = 1.0$, $h\omega^2/g = 2.0$, $\bar{\chi} = \bar{\gamma} = 0.01$.)
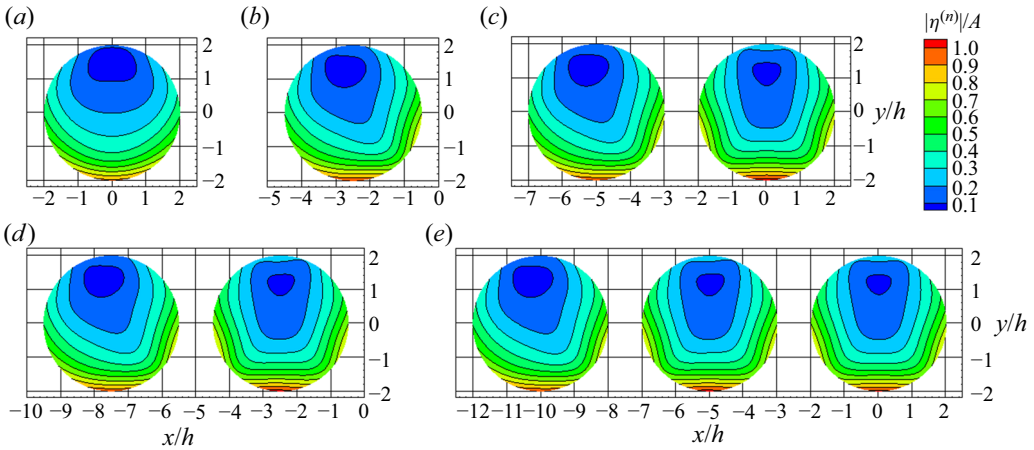

FIGURE 12. Deflection of the plates with a free edge in different cases for different number of plates in the array, N: (a) $N = 1$; (b) $N = 2$; (c) $N = 3$; (d) $N = 4$; (e) $N = 5$. (($x_{j+1} - x_j)/h = 5.0$, $y_j = 0$, $R/h = 2.0$, $\bar{c} = 1.0$, $h\omega^2/g = 2.0$, $\beta = \pi/2$, $\bar{\chi} = \bar{\gamma} = 0.01$.)

The central plate holds a larger overall deflection with $|\eta^{(n)}|_{max}/A = 1.05$, $|\eta^{(n)}|_{min}/A = 0.07$ and two other peak responses ($|\eta^{(n)}|/A = 0.79$) occurring at the edges close to the two side plates. As N increases, responses of the two side plates remain approximately the same, as do the remaining plates in the middle.

Similar changes also apply to the array of plates with a simply supported or clamped-edge condition as shown in figures 13 and 14. In contrast to the free-edge condition, the largest deflection for the simply supported and clamped conditions occurs in the interior of the plate. For the cases of simply supported and clamped-edge conditions with $N \geq 3$, there is an obvious valley of the deflection contour at the central region of each plate except the two side plates, and this valley disappears for the plate with a free-edge condition.

In this paper, a porosity parameter is used to consider the resistance effect induced by the porosity. In fact, this 'resistance effect' acts in much the same way as the 'damping effect',
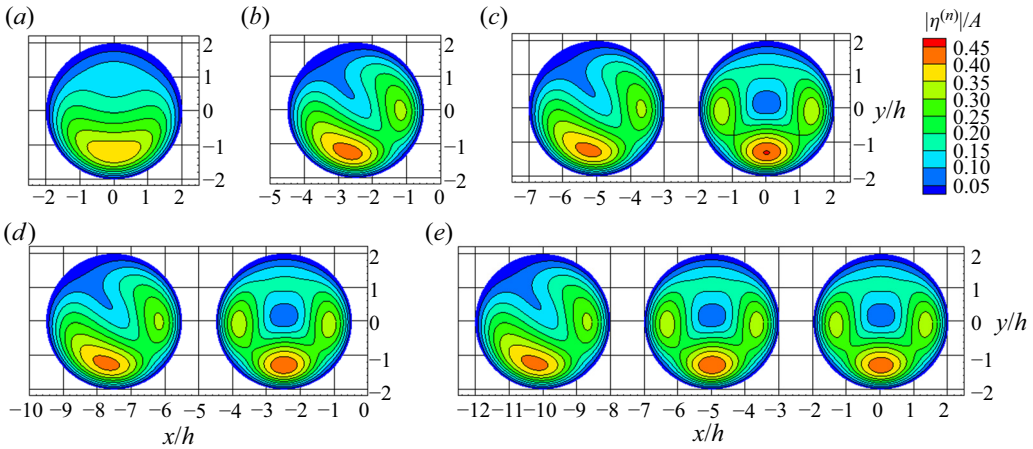
FIGURE 13. Deflection of the plates with a simply supported edge in different cases for different number of plates in the array, N: (a) $N = 1$; (b) $N = 2$; (c) $N = 3$; (d) $N = 4$; (e) $N = 5$. $((x_{j+1} - x_j)/h = 5.0, y_j = 0, R/h = 2.0, \bar{c} = 1.0, h\omega^2/g = 2.0, \beta = \pi/2, \bar{\chi} = \bar{\gamma} = 0.01.)$
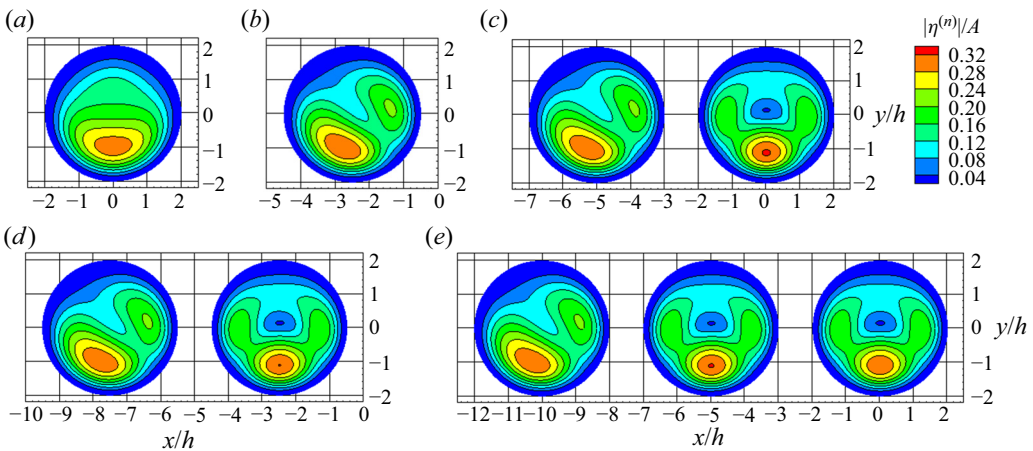

FIGURE 14. Deflection of the plates with a clamped edge in different cases for different number of plates in the array, N: (a) $N = 1$; (b) $N = 2$; (c) $N = 3$; (d) $N = 4$; (e) $N = 5$. $((x_{j+1} - x_j)/h = 5.0, y_j = 0, R/h = 2.0, \bar{c} = 1.0, h\omega^2/g = 2.0, \beta = \pi/2, \bar{\chi} = \bar{\gamma} = 0.01.)$

which has been widely employed to simulate the power takeoff (PTO) of wave-energy converters (WECs). It should be pointed out that the present model for porous elastic plates may be used to simulate the performance of elastic plate-shaped WECs, provided that a special PTO system is designed, which satisfies the surface boundary condition, i.e. (2.4a,b) or (2.5). Indeed, the surface boundary condition employed here is similar to the one Renzi (2016) derived for a piezoelectric plate WEC and also the one Garnaud & Mei (2010) derived for arrays of small buoys. Thus, the corresponding wave-power dissipation can be used to denote the corresponding wave-power absorption of the elastic plate-shaped WECs being consumed by the PTO damping. For a conventional single WEC consisting of an axisymmetric rigid body with heave motion as the only mode of oscillation, the maximum relative absorption width, i.e. η_{diss}, is 1.0 (see, e.g., Budal & Falnes 1975;

Evans 1976). Note that when a porous elastic plate works as a WEC, $\eta_{diss} > 2.0$ and even $\eta_{diss} > 4.0$ are obtained over a large range of circumstances, such as porosity parameters (figure 9), wave frequencies (figure 10) and incident wave direction (figure 11), absorbing more than twice, and even four times, as much wave power as a conventional heaving cylinder can ever achieve. The wave-power absorption can be further enhanced when several elastic circular plates deployed in an array due to the constructive hydrodynamic interaction between them (i.e. the wave power absorbed by the array is larger than that produced by those plates working in isolation), indicating the profound potential of elastic plates for wave-power extraction.

A typical case of an elastic plate-shaped WEC is the piezoelectric plate WEC, which consists of piezoelectric layers bonded to both faces of a flexible substrate. The tension variations at the plate–water interface can be converted into a voltage by the piezoceramic layers owing to the piezoelectric effect, and in this way, the elastic motion excited by water waves is transformed into useful electricity (see e.g. Renzi 2016).

7. Conclusions

A theoretical model based on linear potential flow theory and the eigenfunction matching method has been developed to investigate the interaction of waves with an array of circular floating porous elastic plates. This model can be used to represent artificial marine structures, such as floating flexible breakwaters, artificial floating vegetation fields, and large aquaculture farms with small draught relative to their horizontal dimension. It also provides a possible model for ice floes or flexible plate WECs in which the energy dissipation or wave-power absorption and scattering can be included in a unified way. Graf's addition theorem was applied to consider the hydrodynamic interaction between the plates. The edge condition of the plates can be free, simply supported or clamped.

The response of a pair of porous/non-porous elastic plates predicted by the present theoretical model agreed well with the published theoretical and experimental data, which gave confidence in the current model for solving wave scattering by an array of circular floating porous elastic plates.

Using Green's theorem, it has been proved that the exact wave power dissipated by the plates due to porosity can be evaluated indirectly by using the spatial potentials in the exterior region in terms of the Kochin functions, without consideration of the evanescent waves. This indirect method was shown to produce the same wave-power dissipation as the straightforward method, which takes the area integrals of the unit area dissipated power over all plates with the effect of both propagating and evanescent waves included. The excellent agreement between them gives confidence in the ability of the present theoretical model to calculate wave dissipation by multiple circular floating porous elastic plates.

A multiparameter impact analysis was carried out by applying the validated theoretical model. The main findings are as follows.

(i) For a pair of plates with $R/h = 2.0$, $R_{1,2}/h = 6.0$ and $h\omega^2/g = 2.0$, the wave incident direction corresponding to the maximum wave-power dissipation remains around $\beta/\pi = 0.3$ for all the three different edge conditions.

(ii) In the computed range of $\bar{c}$ (i.e. $\bar{c} < 4.0$) and $R_{1,2}/h$ (i.e. $5.0 \leq R_{1,2}/h \leq 8.0$) with $R/h = 2.0$, $h\omega^2/g = 2.0$, $\beta = \pi/2$, the largest η_{diss} occurs at $R_{1,2}/h = 5.0$ regardless of the types of the plate edges.

(iii) For a row of plates with $R/h = 2.0$, $R_{j,j+1}/h = 5.0$, $h\omega^2/g = 2.0$ and $\beta = \pi/2$, the $\eta_{diss}/N - \bar{c}$ curve rises with the increase of N. The most significant improvement

of η_{diss}/N occurs when N increases from 1 to 2. This also applies to the frequency response of η_{diss}/N with $\bar{c} = 1.0$.

(iv) For the incident waves incoming roughly perpendicular to the row of plates, hydrodynamic interaction between the plates plays a constructive role in dissipating wave power, and the effect strengthens with more plates included in the array. By contrast, if the incident waves propagate along the row of plates, a destructive effect of hydrodynamic interaction on wave-power dissipation is obtained, and the negative influence becomes stronger as the array size increases.

(v) There is a profound potential of elastic plates for wave-power extraction provided that a special PTO system is designed. An elastic plate-shaped WEC is found to capture more than twice, and even four times, as much wave power as a conventional axisymmetric heaving cylinder can ever achieve over a large range of circumstances. Due to the constructive hydrodynamic interaction between the plates in an array, wave-power absorption of the plates can be further enhanced.

Finally, we note that the present theoretical model is developed in the framework of potential flow theory; hence it may not be suitable for the extreme wave–structure interactions.

Acknowledgements

Declaration of interests

The authors report no conflict of interest.

Appendix A. Derivation process of the formulas and calculation for the unknown coefficients $A_{m,l}^{(n)}$ and $B_{m,l}^{(n)}$

Here we take the case of an array of circular floating porous elastic plates with free-edge condition as an example to show how to determine the unknown coefficients $A_{m,l}^{(n)}$ and $B_{m,l}^{(n)}$. Inserting the expression of the spatial potentials for both the exterior and interior regions, i.e. (3.4)–(3.5), into continuity conditions at the interfaces and the free-edge boundary conditions, (2.9a,b) and (3.7)–(3.8), gives

$$
-\frac{igA}{\omega}Z_0(z)\,e^{ik(x_n\cos\beta+y_n\sin\beta)}\sum_{m=-\infty}^{\infty}i^m\,e^{-im\beta}J_m(kR_n)\,e^{im\theta_n}
$$

$$
+\sum_{m=-\infty}^{\infty}\sum_{l=0}^{\infty}A_{m,l}^{(n)}H_m(k_lR_n)Z_l(z)\,e^{im\theta_n}
$$

$$
+\sum_{\substack{j=1,\\j\neq n}}^{N}\sum_{m=-\infty}^{\infty}\sum_{l=0}^{\infty}A_{m,l}^{(j)}Z_l(z)\sum_{m'=-\infty}^{\infty}(-1)^{m'}H_{m-m'}(k_lR_{n,j})J_{m'}(k_lR_n)\,e^{i(m\alpha_{j,n}-m'\alpha_{n,j})}\,e^{im'\theta_n}
$$

$$= \sum_{m=-\infty}^{\infty} \sum_{l=-2}^{\infty} B_{m,l}^{(n)} J_m(\kappa_l R_n) Y_l(z) \, e^{im\theta_n}, \quad -h < z < 0, \tag{A 1}$$

$$- \frac{igA}{\omega} Z_0(z) \, e^{ik(x_n \cos \beta + y_n \sin \beta)} \sum_{m=-\infty}^{\infty} i^m \, e^{-im\beta} k J_m'(kR_n) \, e^{im\theta_n}$$

$$+ \sum_{m=-\infty}^{\infty} \sum_{l=0}^{\infty} A_{m,l}^{(n)} k_l H_m'(k_l R_n) Z_l(z) \, e^{im\theta_n}$$

$$+ \sum_{\substack{j=1, \\ j \neq n}}^{N} \sum_{m=-\infty}^{\infty} \sum_{l=0}^{\infty} A_{m,l}^{(j)} k_l Z_l(z) \sum_{m'=-\infty}^{\infty} (-1)^{m'} H_{m-m'}(k_l R_{n,j}) J_{m'}'(k_l R_n) \, e^{i(m\alpha_{j,n} - m'\alpha_{n,j})} \, e^{im'\theta_n}$$

$$= \sum_{m=-\infty}^{\infty} \sum_{l=-2}^{\infty} B_{m,l}^{(n)} \kappa_l J_m'(\kappa_l R_n) Y_l(z) \, e^{im\theta_n}, \quad -h < z < 0, \tag{A 2}$$

$$\sum_{m=-\infty}^{\infty} \sum_{l=-2}^{\infty} \frac{B_{m,l}^{(n)} f_M(n, m, l)}{\chi \kappa_l^4 + 1 - (\omega^2/g)\gamma} e^{im\theta_n} = 0, \tag{A 3}$$

$$\sum_{m=-\infty}^{\infty} \sum_{l=-2}^{\infty} \frac{B_{m,l}^{(n)} f_V(n, m, l)}{\chi \kappa_l^4 + 1 - (\omega^2/g)\gamma} e^{im\theta_n} = 0, \tag{A 4}$$

where

$$f_M(n, m, l) = R_n^2 \kappa_l^2 J_m''(\kappa_l R_n) - m^2 \upsilon J_m(\kappa_l R_n) + R_n \kappa_l \upsilon J_m'(\kappa_l R_n), \tag{A 5}$$

$$f_V(n, m, l) = R_n^3 \kappa_l^3 J_m'''(\kappa_l R_n) - (2 - \upsilon) R_n m^2 \kappa_l J_m'(\kappa_l R_n)$$

$$+ R_n^2 \kappa_l^2 J_m''(\kappa_l R_n) - (\upsilon - 3) m^2 J_m(\kappa_l R_n) - R_n \kappa_l J_m'(\kappa_l R_n). \tag{A 6}$$

After multiplying both sides of (A 1)–(A 2) by $Z_\zeta(z) \, e^{-i\tau\theta_n}$, integrating in $z \in [-h, 0]$ and $\theta_n \in [0, 2\pi]$ and using their orthogonality characteristics, (A 1)–(A 2) can be rewritten as

$$A_{\tau,\zeta}^{(n)} H_\tau(k_\zeta R_n) A_\zeta + \sum_{\substack{j=1, \\ j \neq n}}^{N} \sum_{m=-\infty}^{\infty} A_{m,\zeta}^{(j)} A_\zeta (-1)^\tau H_{m-\tau}(k_\zeta R_{n,j}) J_\tau(k_\zeta R_n) \, e^{i(m\alpha_{j,n} - \tau\alpha_{n,j})}$$

$$- \sum_{l=-2}^{\infty} B_{\tau,l}^{(n)} J_\tau(\kappa_l R_n) Y_{l,\zeta} = \frac{igA}{\omega} \delta_{0,\zeta} A_\zeta \, e^{ik(x_n \cos \beta + y_n \sin \beta)} i^\tau \, e^{-i\tau\beta} J_\tau(kR_n), \tag{A 7}$$

$$A_{\tau,\zeta}^{(n)} k_\zeta H_\tau'(k_\zeta R_n) A_\zeta + \sum_{\substack{j=1, \\ j \neq n}}^{N} \sum_{m=-\infty}^{\infty} A_{m,\zeta}^{(j)} A_\zeta (-1)^\tau H_{m-\tau}(k_\zeta R_{n,j}) k_\zeta J_\tau'(k_\zeta R_n) \, e^{i(m\alpha_{j,n} - \tau\alpha_{n,j})}$$

$$- \sum_{l=-2}^{\infty} B_{\tau,l}^{(n)} \kappa_l J_\tau'(\kappa_l R_n) Y_{l,\zeta} = \frac{igA}{\omega} \delta_{0,\zeta} A_\zeta \, e^{ik(x_n \cos \beta + y_n \sin \beta)} i^\tau \, e^{-i\tau\beta} k J_\tau'(kR_n), \tag{A 8}$$

where

$$A_l = \int_{-h}^{0} Z_l^2(z)\, \mathrm{d}z = \frac{\sinh(k_l h)\cosh(k_l h) + k_l h}{2 k_l \cosh^2(k_l h)}, \tag{A 9}$$

$$Y_{l,\zeta} = \int_{-h}^{0} Y_l(z) Z_\zeta(z)\, \mathrm{d}z = \frac{\kappa_l \sinh(\kappa_l h)\cosh(k_\zeta h) - k_\zeta \cosh(\kappa_l h)\sinh(k_\zeta h)}{(\kappa_l^2 - k_\zeta^2)\cosh(\kappa_l h)\cosh(k_\zeta h)}. \tag{A 10}$$

In a similar way, after multiplying both sides of (A 3)–(A 4) by $\mathrm{e}^{-\mathrm{i}\tau\theta_n}$ and integrating in $\theta_n \in [0, 2\pi]$, (A 3)–(A 4) can be rewritten as

$$\sum_{l=-2}^{\infty} \frac{B_{\tau,l}^{(n)} f_M(n, \tau, l)}{\chi \kappa_l^4 + 1 - (\omega^2/g)\gamma} = 0, \tag{A 11}$$

$$\sum_{l=-2}^{\infty} \frac{B_{\tau,l}^{(n)} f_V(n, \tau, l)}{\chi \kappa_l^4 + 1 - (\omega^2/g)\gamma} = 0. \tag{A 12}$$

In order to evaluate the unknown coefficients $A_{m,l}^{(n)}$ and $B_{m,l}^{(n)}$, we truncate all infinite series of vertical eigenfunctions at L, i.e. $(L+1)$ terms $(l = 0, 1, \ldots, L)$ for $A_{m,l}^{(n)}$ and $(L+3)$ terms $(l = -2, -1, 0, 1, \ldots, L)$ for $B_{m,l}^{(n)}$, and we take $(2M+1)$ terms $(m = -M, \ldots, 0, \ldots, M)$, resulting in $2N(2M+1)(L+2)$ unknown coefficients to be determined. After taking $(\tau = -M, \ldots, 0, \ldots, M)$ and $(\zeta = 0, 1, \ldots, L)$ in (A 7)–(A 8) and (A 11)–(A 12), a $2N(2M+1)(L+2)$-order complex linear equation matrix is obtained, which can be used to determine the exact same number of unknown coefficients. Here, M and L should be chosen large enough to lead to accurate results. In all the theoretical computations as given in this paper, $M = 10$ and $L = 10$ are used.

REFERENCES

ABRAMOWITZ, M. & STEGUN, I. A. 1972 *Handbook of Mathematical Functions with Formulas, Graphs, and Mathematical Tables*. Government Printing Office.

BEHERA, H. & SAHOO, T. 2015 Hydroelastic analysis of gravity wave interaction with submerged horizontal flexible porous plate. *J. Fluids Struct.* **54**, 643–660.

BENNETTS, L. G., PETER, M. A., SQUIRE, V. A. & MEYLAN, M. H. 2010 A three-dimensional model of wave attenuation in the marginal ice zone. *J. Geophys. Res.* **115**, C12043.

BUDAL, K. & FALNES, J. 1975 A resonant point absorber of ocean-wave power. *Nature* **256**, 478–479.

EVANS, D. V. 1976 A theory for wave-power absorption by oscillating bodies. *J. Fluid Mech.* **77** (1), 1–25.

EVANS, D. V. & PORTER, R. 2003 Wave scattering by narrow cracks in ice sheets floating on water of finite depth. *J. Fluid Mech.* **484**, 143–165.

FÀBREGAS FLAVIÀ, F. & MEYLAN, M. H. 2019 An extension of general identities for 3D water-wave diffraction with application to the diffraction transfer matrix. *Appl. Ocean Res.* **84**, 279–290.

FALNES, J. 2002 *Ocean Waves and Oscillating Systems: Linear Interactions Including Wave-Energy Extraction*. Cambridge University Press.

FANG, Z., XIAO, L. & PENG, T. 2017 Generalized analytical solution to wave interaction with submerged multi-layer horizontal porous plate breakwaters. *J. Engng Maths* **105** (1), 117–135.

FOX, C. & SQUIRE, V. A. 1994 On the oblique reflexion and transmission of ocean waves at shore fast sea ice. *Phil. Trans. R. Soc. Lond.* A **347** (1682), 185–218.

GARNAUD, X. & MEI, C. C. 2010 Bragg scattering and wave-power extraction by an array of small buoys. *Proc. R. Soc. Lond.* A **466** (2113), 79–106.

KAGEMOTO, H. & YUE, D. K. P. 1986 Interactions among multiple three-dimensional bodies in water waves: an exact algebraic method. *J. Fluid Mech.* **166**, 189–209.

KALYANARAMAN, B., BENNETTS, L. G., LAMICHHANE, B. & MEYLAN, M. H. 2019 On the shallow-water limit for modelling ocean-wave induced ice-shelf vibrations. *Wave Motion* **90**, 1–16.

KAMBLE, R. & PATIL, D. 2012 Artificial floating island: solution to river water pollution in India. case study: rivers in Pune city. In *Proceedings of the International Conference on Environmental, Biomedical and Biotechnology, Dubai, UAE*, pp. 136–140. IACSIT.

KOHOUT, A. L., MEYLAN, M. H., SAKAI, S., HANAI, K., LEMAN, P. & BROSSARD, D. 2007 Linear water wave propagation through multiple floating elastic plates of variable properties. *J. Fluids Struct.* **23**, 649–663.

KOLEY, S., MONDAL, R. & SAHOO, T. 2018 Fredholm integral equation technique for hydroelastic analysis of a floating flexible porous plate. *Eur. J. Mech.* B*/Fluids* **67**, 291–305.

LAMAS-PARDO, M., IGLESIAS, G. & CARRAL, L. 2015 A review of very large floating structures (VLFS) for coastal and offshore uses. *Ocean Engng* **109**, 677–690.

LI, Z. F., WU, G. X. & JI, C. Y. 2018*a* Interaction of wave with a body submerged below an ice sheet with multiple arbitrarily spaced cracks. *Phys. Fluids* **30** (5), 057107.

LI, Z. F., WU, G. X. & JI, C. Y. 2018*b* Wave radiation and diffraction by a circular cylinder submerged below an ice sheet with a crack. *J. Fluid Mech.* **845**, 682–712.

MAHMOOD-UL-HASSAN, M., MEYLAN, M. H. & PETER, M. A. 2009 Water-wave scattering by submerged elastic plates. *Q. J. Mech. Appl. Maths* **62** (3), 321–344.

MEYLAN, M. H. 2002 Wave response of an ice floe of arbitrary geometry. *J. Geophys. Res.* **107** (C1), 3005.

MEYLAN, M. H., BENNETTS, L. G. & PETER, M. A. 2017 Water-wave scattering and energy dissipation by a floating porous elastic plate in three dimensions. *Wave Motion* **70**, 240–250.

MEYLAN, M. H. & SQUIRE, V. A. 1996 Response of a circular ice floe to ocean waves. *J. Geophys. Res.* **101** (C4), 8869–8884.

MICHAILIDES, C. & ANGELIDES, D. C. 2012 Modeling of energy extraction and behavior of a flexible floating breakwater. *Appl. Ocean Res.* **35**, 77–94.

MOHAPATRA, S. C., SAHOO, T. & GUEDES SOARES, C. 2018*a* Interaction between surface gravity wave and submerged horizontal flexible structures. *J. Hydrodyn.* **30** (3), 481–498.

MOHAPATRA, S. C., SAHOO, T. & GUEDES SOARES, C. 2018*b* Surface gravity wave interaction with a submerged horizontal flexible porous plate. *Appl. Ocean Res.* **78**, 61–74.

MONTIEL, F., BENNETTS, L. G., SQUIRE, V. A., BONNEFOY, F. & FERRANT, P. 2013*a* Hydroelastic response of floating elastic discs to regular waves. Part 2. Modal analysis. *J. Fluid Mech.* **723**, 629–652.

MONTIEL, F., BONNEFOY, F., FERRANT, P., BENNETTS, L. G., SQUIRE, V. A. & MARSAULT, P. 2013*b* Hydroelastic response of floating elastic discs to regular waves. Part 1. Wave basin experiments. *J. Fluid Mech.* **723**, 604–628.

MONTIEL, F. & SQUIRE, V. A. 2017 Modelling wave-induced sea ice break-up in the marginal ice zone. *Proc. R. Soc. Lond.* A **473** (2206), 20170258.

MONTIEL, F., SQUIRE, V. A. & BENNETTS, L. G. 2015*a* Evolution of directional wave spectra through finite regular and randomly perturbed arrays of scatterers. *SIAM J. Appl. Maths* **75** (2), 630–651.

MONTIEL, F., SQUIRE, V. A. & BENNETTS, L. G. 2015*b* Reflection and transmission of ocean wave spectra by a band of randomly distributed ice floes. *Ann. Glaciol.* **56** (69), 315–322.

MONTIEL, F., SQUIRE, V. A. & BENNETTS, L. G. 2016 Attenuation and directional spreading of ocean wave spectra in the marginal ice zone. *J. Fluid Mech.* **790**, 492–522.

PETER, M. A. & MEYLAN, M. H. 2004 Infinite-depth interaction theory for arbitrary floating bodies applied to wave forcing of ice floes. *J. Fluid Mech.* **500**, 145–167.

PETER, M. A. & MEYLAN, M. H. 2009 Water-wave scattering by vast fields of bodies. *SIAM J. Appl. Maths* **70** (5), 1567–1586.

PETER, M. A., MEYLAN, M. H. & CHUNG, H. 2004 Wave scattering by a circular elastic plate in water of finite depth: a closed form solution. *Intl J. Offshore Polar Engng* **14** (2), 81–85.

PETER, M. A., MEYLAN, M. H. & LINTON, C. M. 2006 Water-wave scattering by a periodic array of arbitrary bodies. *J. Fluid Mech.* **548**, 237–256.

PORTER, R. & EVANS, D. V. 2006 Scattering of flexural waves by multiple narrow cracks in ice sheets floating on water. *Wave Motion* **43** (5), 425–443.

RENZI, E. 2016 Hydroelectromechanical modelling of a piezoelectric wave energy converter. *Proc. R. Soc. Lond.* A **472**, 20160715.

SAHOO, T., YIP, T. L. & CHWANG, A. T. 2001 Scattering of surface waves by a semi–infinite floating elastic plate. *Phys. Fluids* **13** (11), 3215.

SQUIRE, V. A. 2008 Synergies between VLFS hydroelasticity and sea-ice research. In *The Eighteenth International Offshore and Polar Engineering Conference*, pp. 1–13. International Society of Offshore and Polar Engineers.

SQUIRE, V. A. 2011 Past, present and impendent hydroelastic challenges in the polar and subpolar seas. *Phil. Trans. R. Soc. Lond.* A **369** (1947), 2813–2831.

SQUIRE, V. A. 2020 Ocean wave interactions with sea ice: a reappraisal. *Annu. Rev. Fluid Mech.* **52**, 37–60.

SQUIRE, V. A. & DIXON, T. W. 2000 An analytic model for wave propagation across a crack in an ice sheet. *Intl J. Offshore Polar Engng* **10** (03), 173–176.

SQUIRE, V. A. & DIXON, T. W. 2001 How a region of cracked sea ice affects ice-coupled wave propagation. *Ann. Glaciol.* **33**, 327–332.

SUTHERLAND, G., RABAULT, J., CHRISTENSEN, K. H. & JENSEN, A. 2019 A two layer model for wave dissipation in sea ice. *Appl. Ocean Res.* **88**, 111–118.

WANG, C. M. & TAY, Z. Y. 2011 Very large floating structures: applications, research and development. *Procedia Engng* **14**, 62–72.

WILLIAMS, T. D. & PORTER, R. 2009 The effect of submergence on the scattering by the interface between two semi-infinite sheets. *J. Fluids Struct.* **25** (5), 777–793.

ZHAO, X. & SHEN, H. H. 2013 Ocean wave transmission and reflection between two connecting viscoelastic ice covers: an approximate solution. *Ocean Model.* **71**, 102–113.

ZHAO, X. & SHEN, H. H. 2018 Three-layer viscoelastic model with eddy viscosity effect for flexural-gravity wave propagation through ice cover. *Ocean Model.* **131**, 15–23.

ZHENG, S., ANTONINI, A., ZHANG, Y., GREAVES, D., MILES, J. & IGLESIAS, G. 2019 Wave power extraction from multiple oscillating water columns along a straight coast. *J. Fluid Mech.* **878**, 445–480.

ZHENG, S., MEYLAN, M. H., FAN, L., GREAVES, D. & IGLESIAS, G. 2020 Wave scattering by a floating porous elastic plate of arbitrary shape: a semi-analytical study. *J. Fluids Struct.* **92**, 102827.

ZHENG, S., ZHANG, Y. & IGLESIAS, G. 2018 Wave–structure interaction in hybrid wave farms. *J. Fluids Struct.* **83**, 386–412.

ZILMAN, G. & MILOH, T. 2000 Hydroelastic buoyant circular plate in shallow water: a closed form solution. *Appl. Ocean Res.* **22**, 191–198.